Supplementary Information

Efficient photocatalytic synthesis of H_2O_2 coupled with 3,4-dihydroisoquinoline by rGO-modified CdS catalysts

Hui-Li Wu[a], Ting-Ting Wang[a], Chang-Long Tan*[b], Ming-Yu Qi[c], Yi-Jun Xu,[a,b] and Zi-Rong Tang*[a,c]

[a] College of Chemistry, State Key Laboratory of Photocatalysis on Energy and Environment, Fuzhou University, Fuzhou 350116, P. R. China

[b] Institute of Fundamental and Frontier Sciences, University of Electronic Science and Technology of China, Chengdu 611731, P. R. China

[c] School of Materials and Energy, University of Electronic Science and Technology of China, Chengdu 611731, P. R. China

* Corresponding authors.

E-mail addresses: cl_tan@uestc.edu.cn (Chang-Long Tan); zrtang@uestc.edu.cn (Zi-Rong Tang).

Table of Contents

Experimental section

Fig. S1. X-ray diffraction (XRD) patterns of CdS and rGO-CdS composites with different rGO mass ratios (denoted as x% rGO-CdS, x = 5, 10 or 15, respectively).

Fig. S2. Gas chromatography-mass (GC-MS) chromatogram of DHIQ and THIQ.

Fig. S3. Mass spectrogram of (a) DHIQ and (b) THIQ.

Fig. S4. (a) UV-vis absorption spectrum of H_2O_2 standard solutions. (b) Calibration curve for H_2O_2 at 350 nm.

Fig. S5. Gas chromatography-mass spectroscopy (GC-MS) chromatogram of THIQ and DHIQ with different reaction times.

Fig. S6. Time-dependent conversion of THIQ.

Fig. S7. Photocatalytic performance with consecutive THIQ addition.

Fig. S8. The scanning electron microscopy (SEM) image of the used 10% rGO-CdS.

Fig. S9. XRD patterns of the fresh and used 10% rGO-CdS.

Fig. S10. UV-vis diffuse reflectance spectroscopy (DRS) of the fresh and used 10% rGO-CdS.

Fig. S11. Control experiments for photocatalytic activity test.

Fig. S12. Tauc plots for optical band gap of CdS.

Fig. S13. Mott-Schottky plots of CdS.

Fig. S14. Schematic diagram of the energy band structures for 10% rGO-CdS.

Fig. S15. Time-dependent in situ diffuse reflectance infrared Fourier transform spectroscopy (DRIFTS) spectra of 10% rGO-CdS in THIQ/CH_3CN solution under illumination in the wavelength range of 800–1400 cm^{-1}.

Fig. S16. Equations for five possible pathways of co-production of DHIQ and H_2O_2.

Table S1. Photocatalytic systems for O_2 reduction to H_2O_2.

Table S2. Photocatalytic systems for DHIQ synthesis.

Table S3. Photocatalytic systems for co-production of H_2O_2 and organic products.

References

Experimental section

Chemicals and materials. Potassium permanganate ($KMnO_4$), sulfuric acid (H_2SO_4), hydrochloric acid (HCl), acetone (C_3H_6O), hydrogen peroxide 30% (H_2O_2), acetonitrile (CH_3CN), ethanol (C_2H_5OH), dimethyl sulfoxide (C_2H_6OS, DMSO), isopropanol (C_3H_8O), carbon tetrachloride (CCl_4), diammonium oxalate monohydate [$(NH_4)_2C_2O_4 \cdot H_2O$] and 5, 5-dimethyl-1-pyrroline-Noxide (DMPO) were supplied by Sinopharm Chemical Reagent Co., Ltd (Shanghai, China). Cadmium acetate dihydrate [$Cd(CH_3COO)_2 \cdot 2H_2O$], p-benzoquinone, L-tryptophan and 3,4-dihydroisoquinoline (C_9H_9N, DHIQ) were procured from Aladdin Biochemical Technology Co., Ltd (Shanghai, China). Graphite powder was supplied by Zhongtian Co., Ltd. (Qingdao, China). 1,2,3,4-tetrahydroisoquinoline ($C_9H_{11}N$, THIQ) was bought from Bide Pharmatech Co., Ltd (Shanghai, China). Deionized (DI) water was obtained locally.

Synthesis of Graphene oxide (GO). The rGO nanosheets were prepared according to previously reported method.[S1] Specifically, 10 g graphite powder was suspended in 230 mL concentrated H_2SO_4 under moderate agitation. Subsequently, 30 g $KMnO_4$ was added incrementally while maintaining the temperature below 5 °C via an ice bath. The mixture was then heated to 35 °C in a water bath and stirred for 2 h. After that, the resulting mixture was diluted with 500 mL DI water in an ice bath to maintain the temperature below 5 °C. After further dilution with 1.5 L DI water, 80 mL 30% H_2O_2 was added to the mixture. The precipitate was isolated via centrifugation and rinsed with a 1:10 HCl aqueous solution to remove metal ions, followed by repeated DI water rinses until neutral pH was achieved. The washed material was then dialyzed for one week, and the final GO sample was obtained after thorough sonication. Before use, the GO solution should be put in a freeze dryer for 48 h to make it become fluffy GO solid.

Synthesis of x% rGO-CdS composites. A series of rGO-CdS composites with different GO weight percentages (x% rGO-CdS, x = 5, 10 or 15) were synthesized by a simple solvothermal method, during which GO not only served as a support but was also reduced to rGO.[S2] Briefly, specific amounts of GO powders were uniformly dispersed in 60 mL DMSO, and the mixture was then by ultrasonication for 30 min to form a stable dark brown suspension. Subsequently, 0.3998 g of $Cd(CH_3COO)_2 \cdot 2H_2O$, acting as the cadmium source, was added to the above GO dispersion, with ultrasonication continued for another 30 min to enhance homogeneity. The resulting mixture was then transferred into a Teflon-lined stainless-steel autoclave and heated at 180 °C for 12 h in an oven. Herein, DMSO functioned as both the solvent and the sulfur source as well as reducing agent to convert GO to rGO. After the reaction, the system was naturally cooled to room temperature, and the solid product was collected by high-speed centrifugation (13,000 rpm, 10 min). It was then repeatedly washed with anhydrous ethanol and centrifuged to thoroughly remove residual impurities, yielding green solid rGO-CdS. The washed rGO-CdS was dried overnight in a vacuum oven at 60 °C. Pristine CdS nanoparticles (NPs) were synthesized using identical procedures and conditions except for the omission of GO.

Photocatalytic Tests. The photocatalytic conversion of THIQ to DHIQ coupled with H_2O_2 generation was conducted in a sealed quartz reactor, which was maintained at 20 °C via a condenser water system. Specifically, 10 mg photocatalyst and 0.2 mmol THIQ were added to 10 mL CH_3CN, and the resulting suspension was ultrasonically dispersed for 10 min. Then, a 300 W Xe lamp (PLS-SXE 300D,

Beijing Perfectlight Co., Ltd.) with a light density of 0.43 W cm^{-2} was used for irradiation (λ > 400 nm, 30 min, under ambient air). The light power density was measured by a photoradiometer (PL-MW2000, Beijing Perfectlight Co., Ltd.). A magnetic stirrer was used during the reaction to maintain a uniform dispersion of the solution. After the reaction, the solution was filtered through an organic phase nylon syringe filter (0.22 μm) to obtain a clear reaction solution. The organic product was analyzed by gas chromatography-mass spectroscopy (Shimadzu GC-MS QP 2020, Q-Exactive). The selectivity of DHIQ and conversion of THIQ were calculated according to the following equation:

$$\text{Selectivity}(\%) = \frac{n_{DHIQ}}{n_0 - n_{THIQ}} \times 100\%$$

$$\text{Conversion}(\%) = \frac{n_0 - n_{THIQ}}{n_0} \times 100\%$$

Where n_0 means the amount of THIQ that involved in the system initially; n_{THIQ} and n_{DHIQ} respectively indicate the amounts of THIQ residual and the produced DHIQ after reaction.

The concentration of H_2O_2 was determined by the iodimetry method combined with UV-vis spectroscopy (Thermo Fisher Scientific Genesys 10S UV-vis).[S3] 1 mL of 0.4 mol L^{-1}potassium iodide solution was mixed with 1 mL of 0.1 mol L^{-1} potassium hydrogen phthalate solution. Subsequently, the reaction supernatant separated by centrifugation was added into the resulting mixture. The mixed solution was allowed to stand for more than 30 minutes to ensure that H_2O_2 could fully react with I^- under acidic conditions to generate I_3^-.

$$H_2O_2 + 3I^- + 2H^+ \rightarrow I_3^- + 2H_2O$$

The concentration of I_3^- was quantified via UV–vis spectroscopy by detecting the absorbance at 350 nm, and the total amount of H_2O_2 generated throughout the reaction was thereby calculated. The calibration curves were shown in **Fig. S4**. Before the detection, it has been verified that the reaction components (THIQ, DHIQ, and acetonitrile) exhibit negligible absorbance in UV-Vis spectroscopy measurements and thus do not interfere with the quantification of H_2O_2.

Recycling tests. The photocatalytic recycling tests of 10% rGO-CdS were performed as follows. After the first photocatalytic reaction was completed, the catalyst was collected by centrifugation and rinsed three times with acetonitrile. Subsequently, the photocatalyst was dried under a N_2 purge and used for the second recycling test. All subsequent recycling tests were conducted in the same manner. (Reaction conditions: 0.2 mmol THIQ, 10 mL CH_3CN, λ > 400 nm, 30 min, under ambient air)

Characterization methods. The morphology and elemental distribution of the samples were analyzed by scanning electron microscopy (SEM) on a FEI Nova NANO-SEM 230 spectrophotometer, transmission electron microscopy (TEM), high-resolution TEM (HRTEM) and elemental mapping analysis using a JEOL 2100F instrument at an accelerating voltage of 200 kV. X-ray photoelectron

spectroscopy (XPS) measurements were performed using a Thermo Scientific ESCA Lab 250 spectrometer. In XPS analysis, all the binding energies were calibrated by the C 1s peak at 284.6 eV. The crystal phases of the samples were investigated by X-ray diffraction (XRD) on a Rigaku Miniflex diffractometer with Cu Kα radiation at 40 kV and 40 mA in the 2θ range from 10° to 80°. The optical properties of samples were characterized by ultraviolet-visible (UV-vis) diffuse reflectance spectroscopy (DRS) on an UV-vis spectrophotometer (Thermo Scientific Eolution 200 Series), in which $BaSO_4$ was employed as the internal reflectance standard. Electron paramagnetic resonance (EPR) spectroscopic measurements were performed at room temperature using a Bruker A300 EPR spectrometer. For in situ EPR measurements, 10 mg sample powders were dispersed in a mixed solution of 10 mL CH_3CN containing 0.2 mmol THIQ and 0.1mmol 5,5-dimethyl-1-pyrroline N-oxide (DMPO), which was used as a spin-trapping agent, by ultrasonic treatment. Then, the suspension was injected into a glass capillary and placed in a sealed glass tube under an argon (Ar) atmosphere. The sealed glass tube was placed in the microwave cavity of EPR spectrometer and was irradiated with 300 W Xe lamp (λ > 400 nm) during EPR measurements at room temperature. The diffuse reflectance infrared Fourier transform spectroscopy (DRIFTS) was performed on a Thermo Scientific Nicolet iS 50 FT-IR spectrometer. For in situ FTIR measurement, 20 mg of sample powders were placed onto KBr and 200 μL anhydrous THIQ was added. The reaction system was purged with Ar for 10 min and irradiated with a 300 W Xe lamp.

Photoelectrochemical measurements. The electrochemical and photoelectrochemical measurements were conducted on an electrochemical work station (MUTI AUTOLAB M204) with a conventional three-electrode cell, which used a Pt plate as the counter electrode and an Ag/AgCl electrode as the reference electrode. The working electrode was prepared on fluorine doped tin oxide (FTO) glass that was cleaned by sonication in ethanol for 30 min and dried at 60 °C. Typically, 5 mg of sample was fully dispersed in a mixture of 1 mL N,N-dimethylformamide (DMF) and 50 μL Nafion solution by ultrasonic treatment. The 15 μL slurry was spread onto the exposed area (0.25 cm^2) of the pre-treated FTO glass, whose boundary was protected using scotch tape. After drying at 60 °C for 5 h, the scotch tape was unstuck, and the uncoated part of the electrode was isolated with epoxy resin. The transient photocurrent measurement was conducted in a 0.2 M Na_2SO_4 aqueous solution without an applied voltage bias under the UV-vis light irradiation. Additionally, the cyclic voltammetry (CV) curves and linear sweep voltammetry (LSV) tests were measured in a 0.2 M Na_2SO_4 aqueous solution (pH = 7). The electrochemical impedance spectroscopy (EIS) measurement was carried out in a 0.5 M KCl solution including 0.01 M $K_3[Fe(CN)_6]/K_4[Fe(CN)_6]$. Mott-Schottky plots were obtained at frequencies of 500, 1000 and 1500 Hz with a bias potential ranging from −1 to 2 V vs. Ag/AgCl.

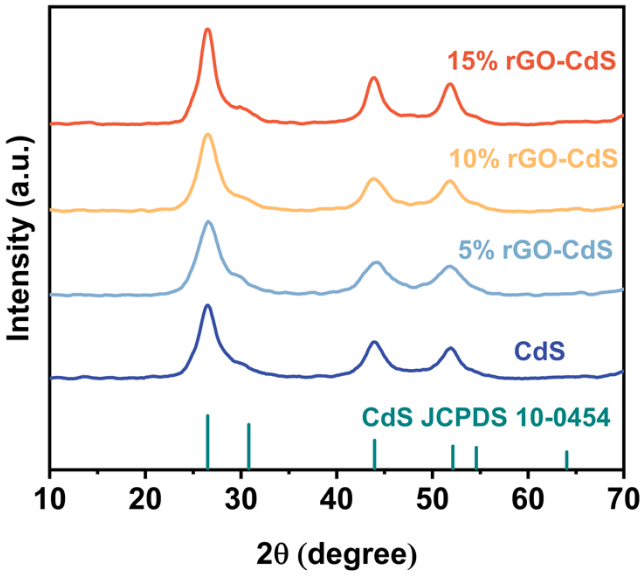

Fig. S1. X-ray diffraction (XRD) patterns of CdS and rGO-CdS composites with different rGO mass ratios (denoted as x% rGO-CdS, x = 5, 10 or 15, respectively).

Note: In the XRD pattern of the rGO-CdS composites, the characteristic diffraction peaks can be exclusively indexed to the hexagonal phase of CdS (JCPDS No. 10-0454). No distinct diffraction peak for rGO is observed, which is a common phenomenon reported in the literature for well-exfoliated and thinly coated rGO on semiconductor substrates. [S1] This absence can be attributed to the reason that the relatively low amount and high dispersion of rGO in the composite, which falls below the detection limit of XRD.

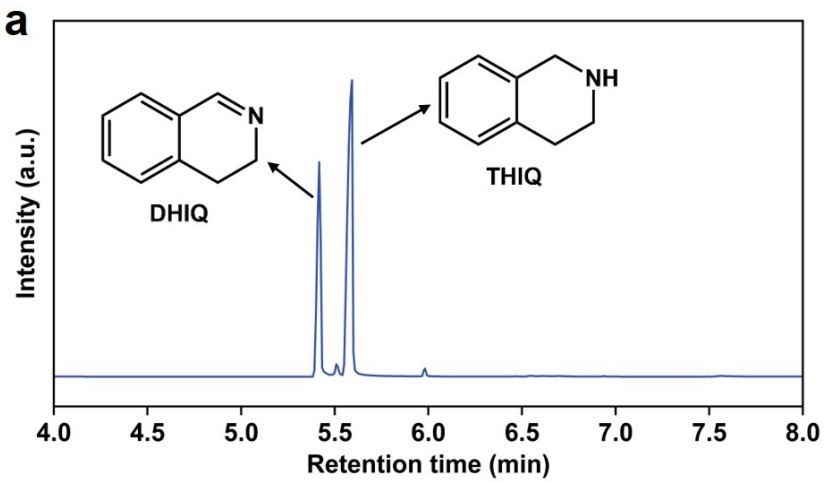

Fig. S2. Gas chromatography-mass spectrometry (GC-MS) chromatogram of DHIQ and THIQ.

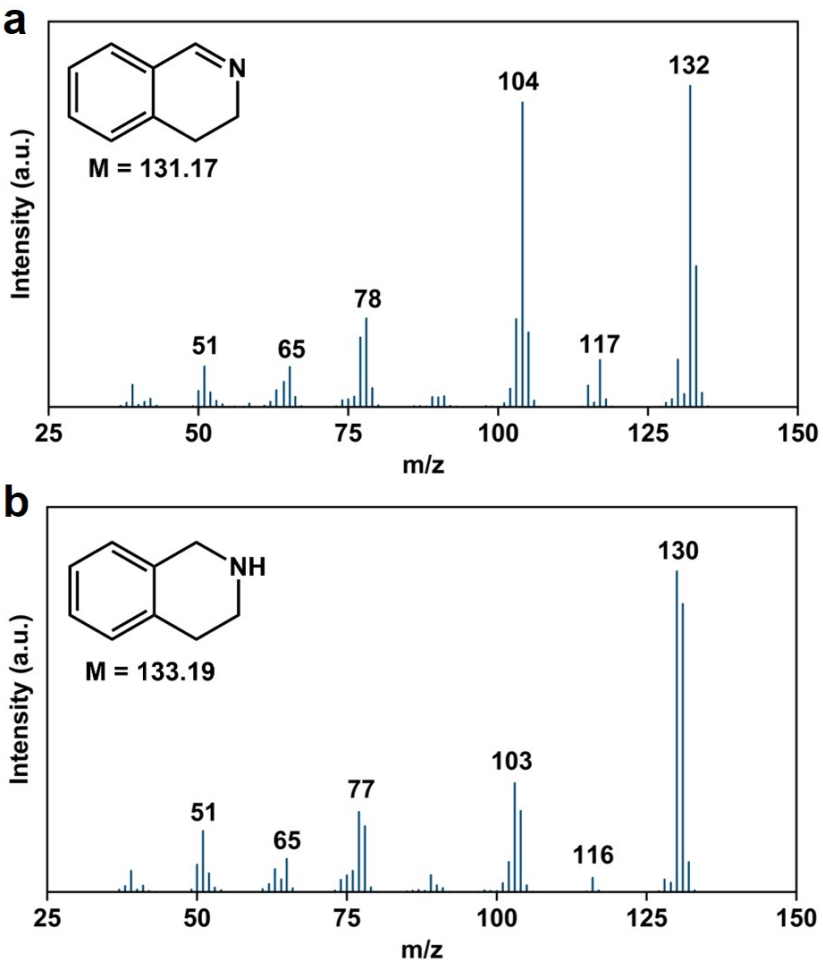

Fig. S3. Mass spectrogram of (a) DHIQ and (b) THIQ.

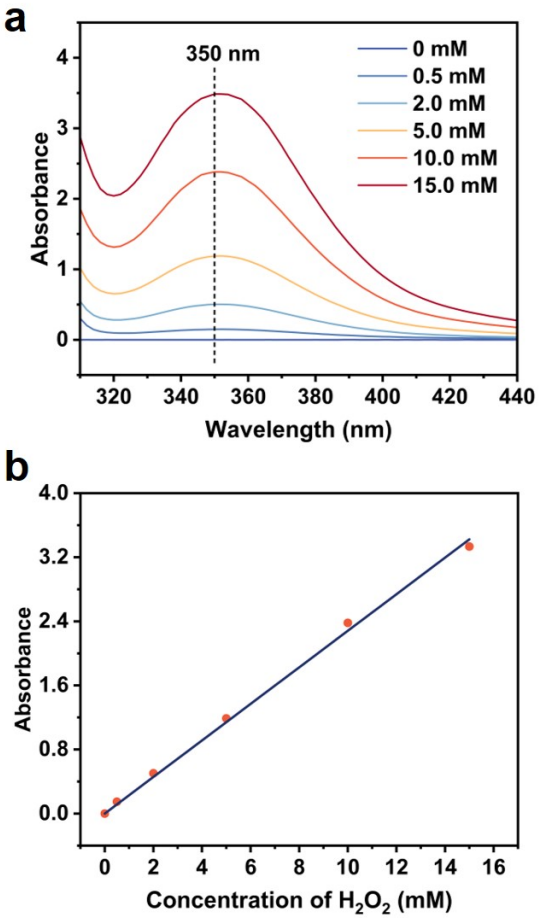

Fig. S4. (a) UV-vis absorption spectrum of H_2O_2 standard solutions. (b) Calibration curve for H_2O_2 at 350 nm.

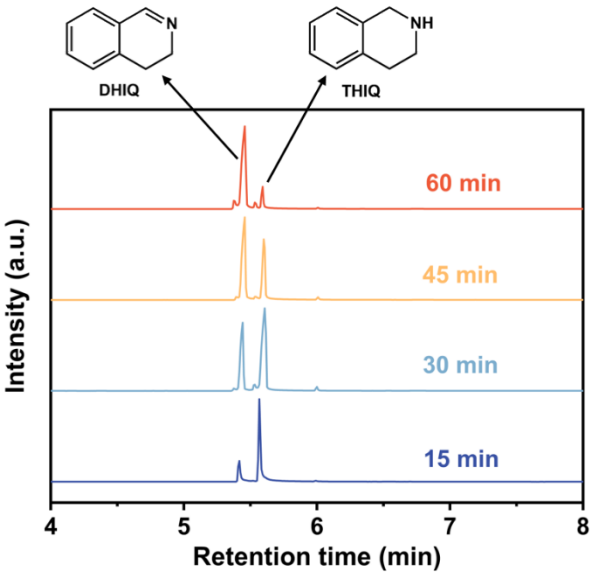

Fig. S5. Gas chromatography-mass spectroscopy (GC-MS) chromatogram of THIQ and DHIQ with different reaction times.

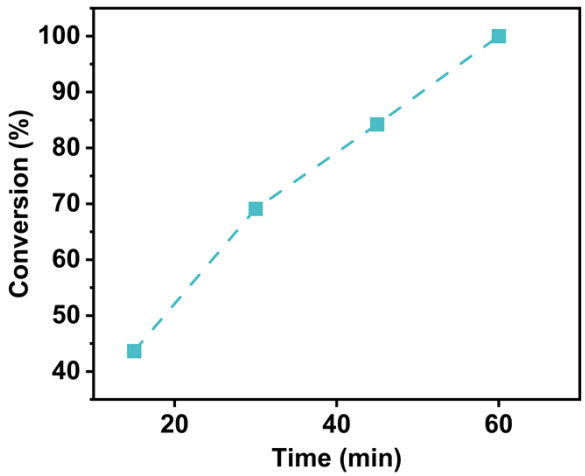

Fig. S6. Time-dependent conversion of THIQ.

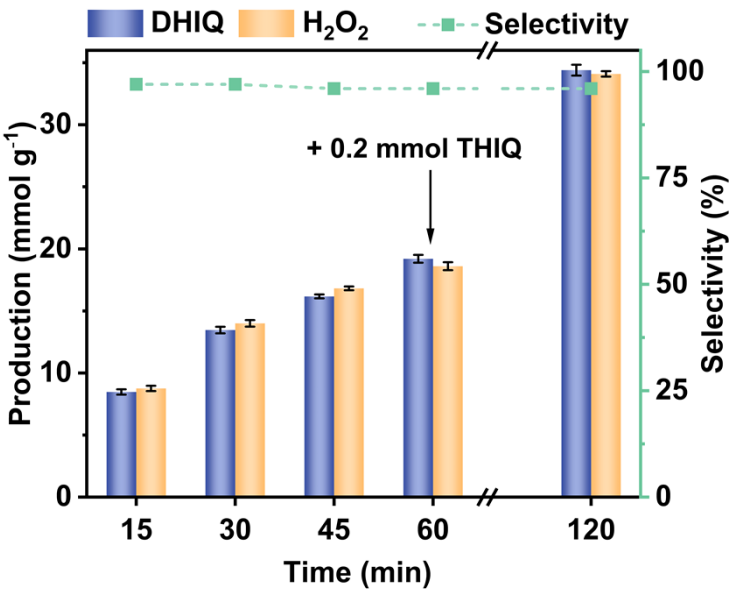

Fig. S7. Photocatalytic performance with consecutive THIQ addition.

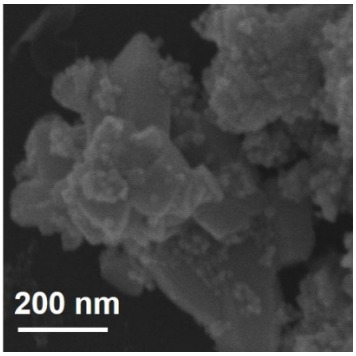

Fig. S8. The scanning electron microscopy (SEM) image of the used 10% rGO-CdS.

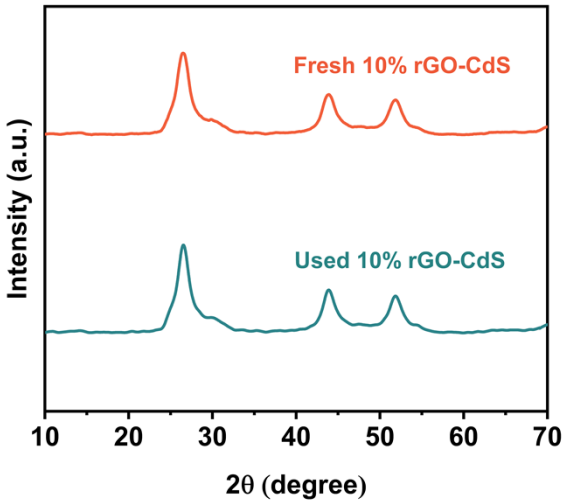

Fig. S9. XRD patterns of the fresh and used 10% rGO-CdS.

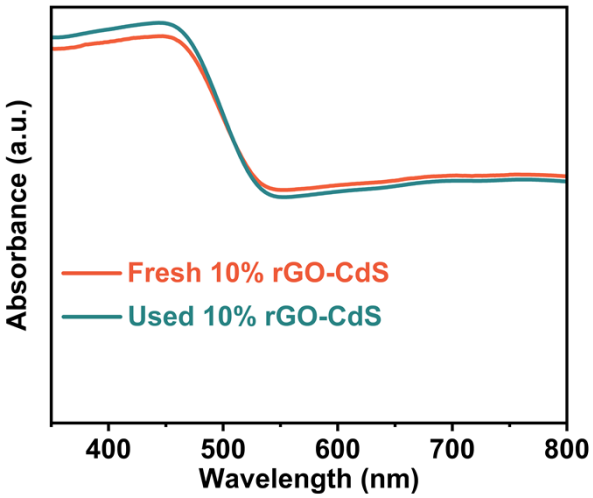

Fig. S10. UV-vis diffuse reflectance spectroscopy (DRS) of the fresh and used 10% rGO-CdS.

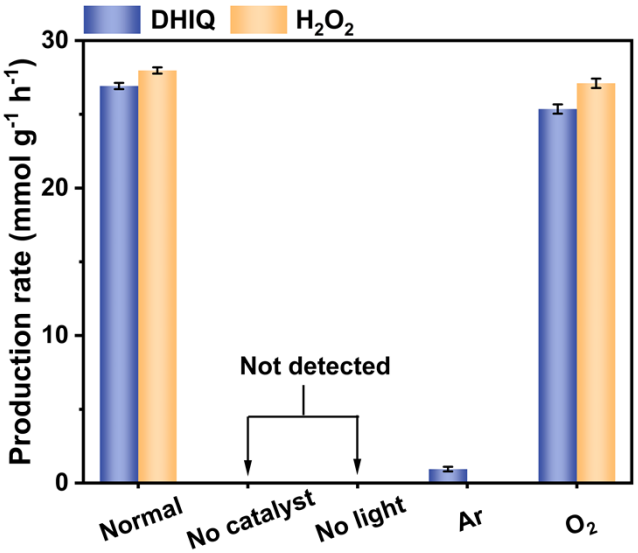

Fig. S11. Control experiments for photocatalytic activity test.

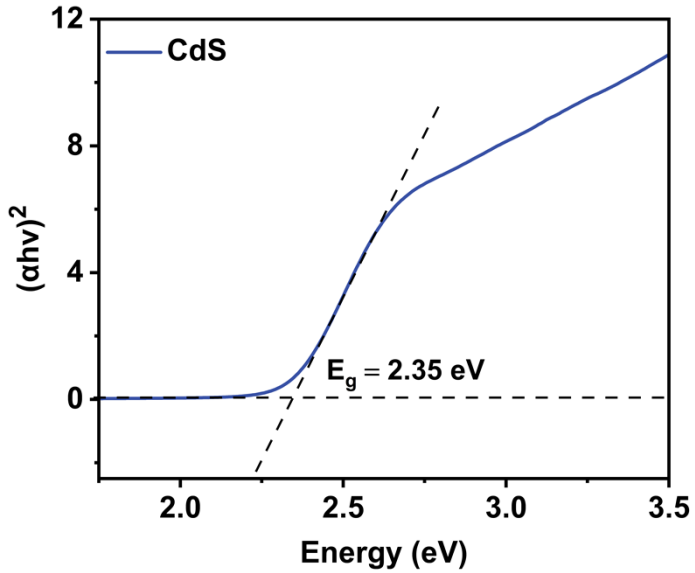

Fig. S12. Tauc plots for optical band gap of CdS.

Note: The band gap energy of CdS and 10% rGO-CdS can be calculated by the transformed Kubelka-Munk function:

$$(\alpha h\nu)^{n} = K \times (h\nu - E_g)$$

where α is the absorption coefficient, $h\nu$ is the photon energy, K is a constant, E_g is the band gap energy and n = 2. In **Fig. S12**, the E_g of pristine CdS is calculated to be 2.35 eV based on the Tauc plots obtained from the transformed Kubelka-Munk function.[S4]

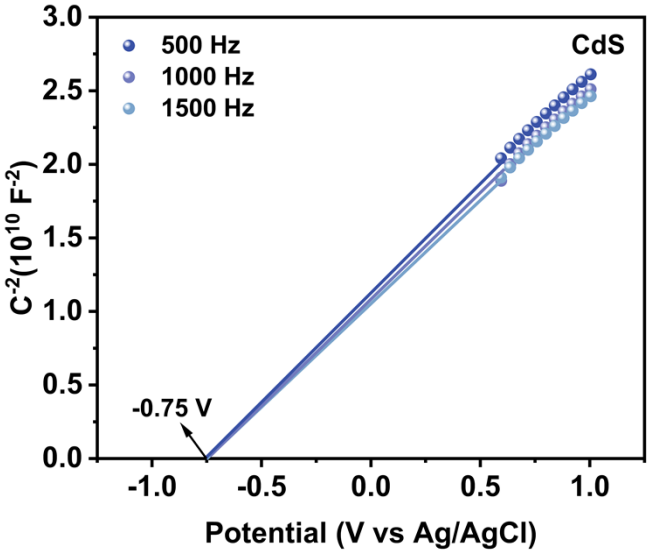

Fig. S13. Mott-Schottky plots of CdS.

Note: The flat band potential (E_{fb}) of CdS, as calculated from the horizontal axis intercept of the linear region, is −0.75 V vs. Ag/AgCl. The Fermi level (E_F) and E_{fb} of semiconductors are equal at the equilibrium state. According to the equation between the normal hydrogen electrode (NHE) and Ag/AgCl ($E_{NHE} = E_{Ag/AgCl} + 0.20$ V), the conduction band (CB) position of CdS is calculated as −0.55 V vs. NHE. On this basis, the valence band (VB) position of CdS is further derived as +1.80 V vs. NHE using the equation $E_{VB} = E_{CB} + E_g$.[S2]

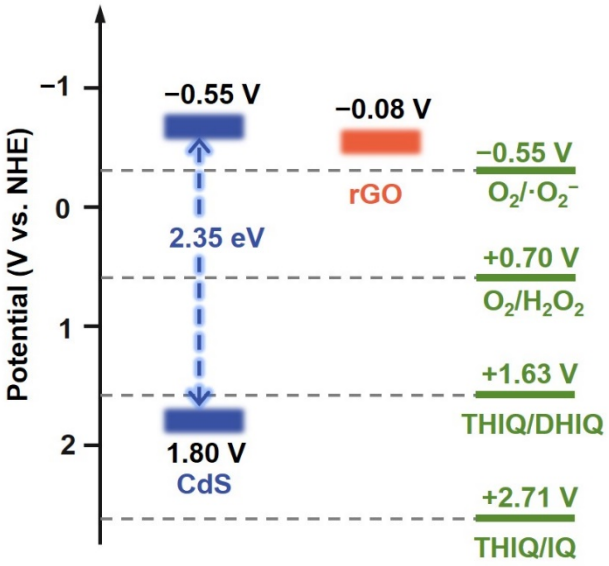

Fig. S14. Schematic diagram of the energy band structures for 10% rGO-CdS.

Note: The band structure diagram in **Fig. S14** reveals that the CB potential of CdS is sufficiently negative to reduce O_2 into superoxide radicals ($^{\bullet}O_2^-$, with $E(O_2/^{\bullet}O_2^-)$ = −0.33 V vs. NHE), while its VB potential (+1.80 V vs. NHE) can oxidize THIQ to produce DHIQ ($E_{(THIQ/DHIQ)}$ = +1.63 V vs. NHE).[S5] Meanwhile, the VB of CdS is insufficient to oxidize THIQ to IQ ($E_{(THIQ/IQ)}$ = +2.71 V vs. NHE), blocking the secondary dehydrogenation and favoring DHIQ as the major product.[S6]

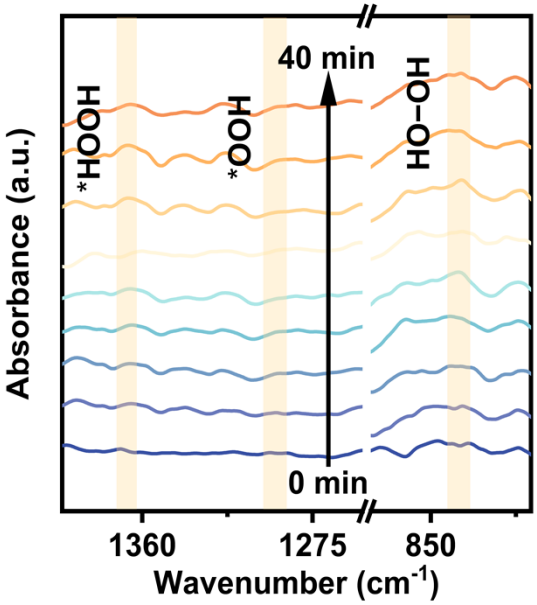

Fig. S15. Time-dependent in situ diffuse reflectance infrared Fourier transform spectroscopy (DRIFTS) spectra of 10% rGO-CdS in THIQ/CH_3CN solution under illumination in the wavelength range of 800–1400 cm^{-1}.

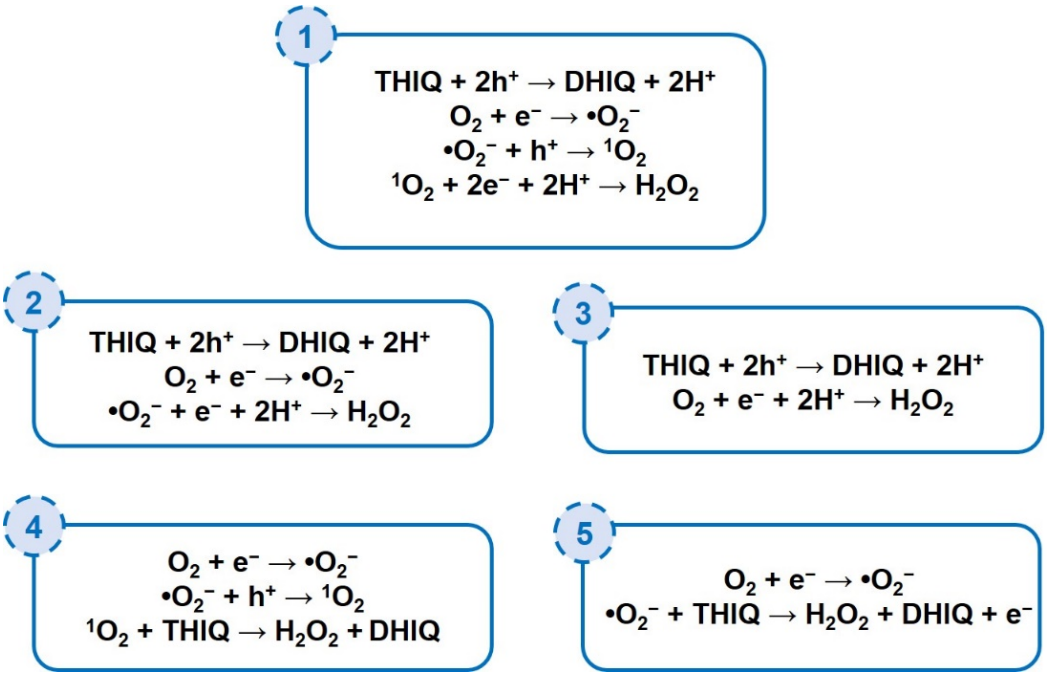

Fig. S16. Equations for five possible pathways of co-production of DHIQ and H_2O_2.[S5]

Table S1. Photocatalytic systems for O_2 reduction to H_2O_2.

Entry	Catalyst	Atmosphere	Light source	H_2O_2 production rate ($mmol \cdot g^{-1} \cdot h^{-1}$)	Ref.
1	rGO-CdS	Air	λ > 400 nm	27.98	This work
2	ZnO-300	O_2	λ ≥ 360 nm	2.79	S7
3	P-mMCNNS-25	O_2	AM1.5G simulated sunlight	1.08	S8
4	TiO_2/In_2S_3-10	O_2	Hg lamp	0.75	S9
5	TiO_2/MoS_x-Au	O_2	Xe lamp	30.44	S10
6	$Au_{0.5}/WO_3$	O_2	λ ≥ 420 nm	0.109	S11
7	OCN-500	O_2	λ ≥ 420 nm	2.92	S12
8	NDCN	O_2	λ ≥ 420 nm	0.048	S13
9	m-CNNP	Air	400–700 nm	0.043	S14
10	Cu(I)-SA/WO_3	O_2	Xe lamp λ > 420 nm	2.04	S15

Table S2. Photocatalytic systems for DHIQ synthesis.

Entry	Catalyst	Atmosphere	Solvent	Light source	DHIQ production rate ($mmol \cdot g^{-1} \cdot h^{-1}$)	Ref.
1	rGO-CdS	Air	CH_3CN	λ > 400 nm	26.32	This work
2	$MoS_2/ZnIn_2S_4$	N_2	CH_3CN/H_2O (3:1)	λ > 420 nm	0.72	S16
3	Pd/CdS	Ar	CH_3CN	λ > 420 nm	0.17	S17
4	ZIS-EG	Air	Dimethylformamide	455 nm LED lamp	1.40	S18
5	triphenylamine-PDI	Air	CH_3CN	420 nm LED lamp	1.68	S19
6	TAPP-An	O_2	CH_3CN	Xe lamp	1.10	S20

Table S3. Photocatalytic systems for co-production of H_2O_2 and organic products.

Entry	Catalyst	Atmosphere	Reagent (mmol)	Light source	H_2O_2 production rate ($mmol \cdot g^{-1} \cdot h^{-1}$)	Organic synthesis rate ($mmol \cdot g^{-1} \cdot h^{-1}$)	Ref.
1	rGO-CdS	Air	THIQ 0.2	λ > 400 nm	27.98	DHIQ 26.32	This work
2	$Zn_3In_2S_6$	O_2	THIQ 0.125	λ ≥ 400 nm	66.4	DHIQ 62.10	S5
3	COF-Py-S	O_2	THIQ 0.65	λ > 400 nm	19.00	DHIQ 16.25	S21
4	$ZrS_{1-y}S_{2-x}$ (15/100)	O_2	Benzylamine 0.1	AM1.5G simulated sunlight	1.56	Benzonitrile 0.64	S22
5	Fe_3O_4@CdS@C QDs	O_2	Pure benzyl alcohol	λ > 300 nm	27.10	Benzaldehyde 57.2	S23
6	Ag@T-C_3N_4	O_2	Benzyl alcohol 119.9	Xe lamp, 420–780 nm	4.73	Benzaldehyde 19.71	S24
7	OPA/Fe-Zr-MOF	O_2	Benzyl alcohol 48.1	λ > 420 nm	5.24	Benzaldehyde 5.83	S25
8	Ti_2O_3/Bi_2O_3-40	O_2	Furfuryl alcohol 0.29	Xe lamp, 350–780 nm	2.88	Furoic acid 1.12	S26
9	DCM-HCPs	Air	Bezylamine 0.2	455 nm LED lamp	5.71	N-Benzylideneben zylamine 13.3	S27
10	JUC-675	O_2	Bezylamine 0.1	Xe lamp λ > 420 nm	22.80	N-Benzylideneben zylamine 9.6	S3
11	Pd(0.05)	O_2	Benzyl alcohol	470 nm	0.006	Benzaldehyde	S28

	/BMO-SOVs		0.1	LED lamp		0.82	
12	TiO_2	O_2	Benzyl alcohol 1.75	Hg lamp λ > 280 nm	0.33	Aldehyde or Ketone 0.33	S29
13	g-C_3N_4	O_2	Ethanol 77.1	λ > 420 nm	0.12	Aldehyde 0.13	S30

References

S1 K.-Q. Lu, Y.-H. Li, F. Zhang, M.-Y. Qi, X. Chen, Z.-R. Tang, Y. M. A. Yamada, M. Anpo, M. Conte and Y.-J. Xu, *Nat. Commun.*, 2020, **11**, 5181.

S2 M.-H. Sun, M.-Y. Qi, Z.-R. Tang and Y.-J. Xu, *App. Catal. B: Environ.*, 2023, **321**, 122019.

S3 J. Liu, C. Tuo, W.-Y. Xiao, M.-Y. Qi, Y. Yusran, Z. Wang, H. Li, C. Guo, J. Song, S. Qiu, Y.-J. Xu and Q. Fang, *Angew. Chem. Int. Ed.*, 2025, **64**, e202416240.

S4 X.-N. Shao, Y.-F. Wang, M.-Y. Qi and Z.-R. Tang, *Mol. Catal.*, 2024, **557**, 113991.

S5 J. Luo, X. Wei, Y. Qiao, C. Wu, L. Li, L. Chen and J. Shi, *Adv. Mater.*, 2023, **35**, 2210110.

S6 L. Chen and J. Shi, *Sci. China Mater.*, 2022, **65**, 1-9.

S7 Y. Zhang, Y. Xia, L. Wang, B. Cheng and J. Yu, *Nanotechnology*, 2021, **32**, 415402.

S8 L. Zhou, J. Feng, B. Qiu, Y. Zhou, J. Lei, M. Xing, L. Wang, Y. Zhou, Y. Liu and J. Zhang, *App. Catal. B: Environ.*, 2020, **267**, 118396.

S9 Y. Yang, B. Cheng, J. Yu, L. Wang and W. Ho, *Nano Res.*, 2023, **16**, 4506-4514.

S10 X. Zhang, D. Gao, B. Zhu, B. Cheng, J. Yu and H. Yu, *Nat. Commun.*, 2024, **15**, 3212.

S11 Y. Wang, Y. Wang, J. Zhao, M. Chen, X. Huang and Y. Xu, *App. Catal. B: Environ.*, 2021, **284**, 119691.

S12 Z. Wei, M. Liu, Z. Zhang, W. Yao, H. Tan and Y. Zhu, *Energy Environ. Sci.*, 2018, **11**, 2581-2589.

S13 J. Luo, Y. Liu, C. Fan, L. Tang, S. Yang, M. Liu, M. Wang, C. Feng, X. Ouyang, L. Wang, L. Xu, J. Wang and M. Yan, *ACS Catal.*, 2021, **11**, 11440-11450.

S14 W. Liu, C. Song, M. Kou, Y. Wang, Y. Deng, T. Shimada and L. Ye, *Chem. Eng. J.*, 2021, **425**, 130615.

S15 F. Yang, C. Feng, S. Zuo, Q. Wang, F. Wei, M. Hu, Y. Ren, D. Liu, W.-L. Li, S. Wang, H. S. Alqahtani, Y. H. Ng and H. Zhang, *J. Am. Chem. Soc.*, 2025, **147**, 17112-17120.

S16 M. Hao, X. Deng, L. Xu and Z. Li, *App. Catal. B: Environ.*, 2019, **252**, 18-23.

S17 Y. Chen, M.-Y. Qi and Z.-R. Tang, *Mol. Catal.*, 2024, **561**, 114178.

S18 X. Yin, B. Lv, Y. Kang, X. Xu, X. Lei, L. Li, H. Wang, H. Xi, J. Yang and Z. Yang, *Catal. Lett.*, 2023, **153**, 570-583.

S19 H. Zhang, K. Yu, Z. Wu and Y. Zhu, *EcoMat*, 2022, **4**, e12215.

S20 Y. Chen, S.-N. Sun, X.-H. Chen, M.-L. Chen, J.-M. Lin, Q. Niu, S.-L. Li, J. Liu and Y.-Q. Lan, *Adv. Mater.*, 2025, **37**, 2413638.

S21 T. Yang, F. Kong, Y. Chen, A. Kong, X. Cui and J. Shi, *Angew. Chem. Int. Ed.*, 2025, **64**, e202424110.

S22 Z. Tian, C. Han, Y. Zhao, W. Dai, X. Lian, Y. Wang, Y. Zheng, Y. Shi, X. Pan, Z. Huang, H. Li and W. Chen, *Nat. Commun.*, 2021, **12**, 2039.

S23 Z. Zheng, F. Han, B. Xing, X. Han and B. Li, *J. Colloid Interface Sci.*, 2022, **624**, 460-470.

S24 X. Zhou, K. Cao, S. Huang, H. Wu, Z. Cao, H. Liu, P. Chen, D. Su, G. Wang, T. Wang, C. Wang and H. Pang, *Angew. Chem. Int. Ed.*, 2025, e202505532.

S25 X. Chen, Y. Kuwahara, K. Mori, C. Louis and H. Yamashita, *ACS Appl. Energy Mater.*, 2021, **4**, 4823-4830.

S26 B. He, Z. Wang, P. Xiao, T. Chen, J. Yu and L. Zhang, *Adv. Mater.*, 2022, **34**, 2203225.

S27 W. Wang, W. Gao, X. Nie, W. Liu, X. Cheng, N. Shang, S. Gao and C. Wang, *J. Colloid Interface Sci.*, 2022, **616**, 1-11.

S28 Z. Sun, X. Yang, X.-F. Yu, L. Xia, Y. Peng, Z. Li, Y. Zhang, J. Cheng, K. Zhang and J. Yu, *App. Catal. B: Environ.*, 2021, **285**, 119790.

S29 Y. Shiraishi, S. Kanazawa, D. Tsukamoto, A. Shiro, Y. Sugano and T. Hirai, *ACS Catal.*, 2013, **3**, 2222-2227.

S30 Y. Shiraishi, S. Kanazawa, Y. Sugano, D. Tsukamoto, H. Sakamoto, S. Ichikawa and T. Hirai, *ACS Catal.*, 2014, **4**, 774-780.